Effect of environmental radiation on the long-wave infrared signature of cruise aircraft

CrossMark

Wei Huang *, Honghu Ji *

Jiangsu Province Key Laboratory of Aerospace Power System, Nanjing University of Aeronautics and Astronautics, Nanjing, Jiangsu, 210016, China

A B S T R A C T

In the long-wave infrared radiation band (8–12 μm), the environmental radiation greatly affects the infrared signature of aircraft. The main aim of this paper is to assess the effects of atmospheric and ground radiance on the infrared signature of a cruise aircraft flying at high altitude. Firstly, the computation method of infrared signature is presented. The reverse Monte Carlo ray tracing method is applied to evaluate the effect of environmental radiation on the infrared signature of aircraft. The MODTRAN code is used to compute the atmospheric/ground radiance and atmospheric transmittance. Then, this method is validated with experimental data. Finally, the effect of environmental radiation on infrared signature of aircraft is discussed with the consideration of atmospheric condition, flight altitude, flight speed, and the emissivity of the airframe skin. The results show that the infrared signature of the lower surface of the aircraft is sensitive to the environmental radiation whose reflection contributes more than 20% to the total radiation at Mach 0.9. Increasing flight altitude, reducing atmosphere temperature and reducing flight speed will increase the ratio of reflected environmental infrared radiation intensity to total infrared radiation intensity of the aircraft. After considering the environmental radiation, the reduction amplitude of infrared signature of the aircraft by reducing the surface emissivity is decreased. The infrared signature of the aircraft lower surface is still significant compared to environment, even though the emissivity of the aircraft surface is reduced.

© 2016 Elsevier Masson SAS. All rights reserved.

1. Introduction

The infrared (IR) signature of an aircraft is one of the most important factors which affect the detection range of an IR detection system [1]. In general, the IR signature of an aircraft is mainly attributed to the following radiation sources [2]: the emission from the airframe surface and the engine hot parts, the emission from the hot plume, and the reflected environmental radiation by the surface of the aircraft. The environmental radiation, mainly includes the radiation form atmosphere, earth surface and the sun [3]. In the long-wave infrared band (8–12 μm), the dominant environmental radiations are atmospheric radiation and earth surface radiation. The relationship between environment and IR signature of a aircraft in three key ways: (1) the environment influences the surface temperature of the airframe, through radiative and convective heat transfer, and then affects the surface emission of the airframe; (2) the environment influences the amount of incident radiation on the airframe surface, in turn influence the reflected radiation from the skin; (3) the environment influences the transmission of the emitted and reflected radiation from the target to an observing sensor.

The atmospheric IR radiation is mainly attributed to the thermal emission of radiating species in atmosphere (such as CO_2, H_2O, and O_3) as well as the scattered radiation by suspended particles in the atmosphere (e.g. aerosols). The radiation of atmosphere is primarily governed by pressure, temperature, and concentration of species CO_2, H_2O, and O_3. The concentration of CO_2 is nearly constant, about 370 ppm. The concentration of H_2O decreases rapidly with the increase of altitude, and is absent above 10 km. The concentration of O_3 is prominent only at an altitude of 20–30 km. In the troposphere, the temperature and pressure decrease with the increase of altitude. In order to facilitate the calculation of the atmospheric radiance and transmissivity, some typical atmospheric IR radiation models are developed, such as 1976 US Standard model, Mid-latitude Summer (45 degrees North, July) model, Mid-latitude Winter (45 degrees North, January) model, etc.

Some simple empirical models, such as Bliss model [4], Kimball model [5], Awanou model [6] and Berger model [7,8], can be used to calculate the atmospheric infrared radiation. However, these models usually are used to calculate the atmospheric radiation near ground, and may not be suitable for the calculation at

high altitude. In addition to those models, the LOWTRAN/MOD-TRAN code [9] are two widely used tools to accurate calculate the environmental radiation and the propagation of infrared radiation through the atmosphere. They are comprehensive empirical-based programs based on band models of molecular absorption, so they have improved accuracy. For the simulation of the emission from the earth surface, the infrared radiation is treated as a function of several parameters, e.g. vegetation, temperature, humidity, type of soil and rock [10]. Most surfaces characterizing the earth are predominantly diffuse and behave as grey bodies with high emissivity ε. Therefore, the earth surface emission could be simulated by using Lambert model [11].

There are a lot of valuable studies about the aircraft IR signature in the long-wave band. Coiro [1] upgraded the CRIRA (Calcul du Rayonnement InfraRouge des Avions) code with a global illumination model and validated it on a Boeing 737 airplane. The global illumination model uses a Monte Carlo Ray Tracer (MCRT) to model the reflection of the natural environment radiation on the aircraft, the emissions and reflections of the airplane on itself. Comparing with experimental data, the accuracy of thermal image was improved with this technique. However, detailed analysis of the effect of environmental infrared radiation on the IR signature of the aircraft was not provided. Harkiss [12] investigated the effect of Bi-directional Reflectance Distribution Function (BRDF) of the aircraft surface and the number of reflection bounces on the IR signature of a large commercial aircraft at takeoff and landing. Li et al. [13] developed a real-time aircraft infrared imaging simulation code, which involves temperature model, infrared radiation model of zero-distance, atmospheric transfer model and infrared imaging system effect model. However, the reflections between different regional surface elements of the airframe surface, and the reflections inside the nozzle cavity seem not to be included in the computation. Mahulikar et al. [10] and Rao et al. [14] investigated the effect of atmospheric radiance on the IR signature of an aircraft flying at altitude of 5 km by using the Berger model [7]. The results showed that the atmospheric radiation plays a significant role to determine the IR signature of the aircraft. Lu et al. [15] investigated the infrared radiation characteristics of the aircraft surface with the computational fluid dynamics (CFD) and the Reverse Monte Carlo (RMC) method. However, the environmental radiation was not considered in the study.

The IR signature of aircraft strongly depends on the flight conditions, the environment properties, the detection aspect angles, and the spectral bands, etc. It seems that, in the literatures, the investigation of the effect of environmental radiation on the IR signature of aircraft is insufficient, especially for an aircraft cruising at high altitude. The main purpose of this paper is to assess the effect of infrared radiation of atmosphere and earth ground on the long-wave band IR signature of a cruise aircraft at high altitude. The effects of flight speeds (Mach 0.9, 1.2 and 1.5), flight altitudes (7 km and 11 km), seasons (winter and summer) as well as the emissivity of the airframe surface on the IR signature are studied in present work.

2. The method of IR signature computation

2.1. Computation procedure of aircraft infrared radiation

The main radiation sources of long wave band IR signature of an aircraft are as follows: (1) the surface of the aircraft; (2) the intake cavity, which is composed of intake duct and the first stage of the low-pressure compressor of the engine; (3) the exhaust cavity, which is composed of the last stage of the turbine and all components downstream it, e.g. mixer, central body, flame holders, afterburner and nozzle, et al.; (4) the exhaust hot gases of the engine. The surface of the aircraft not only emits energy due
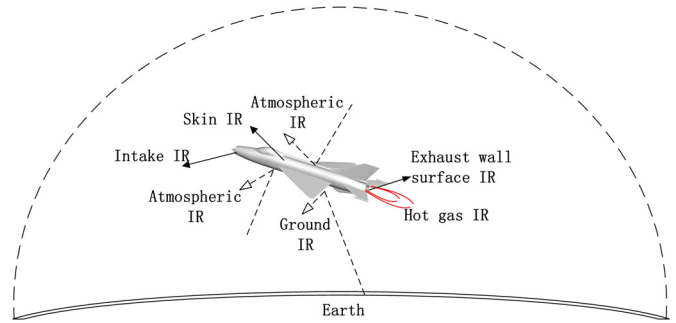

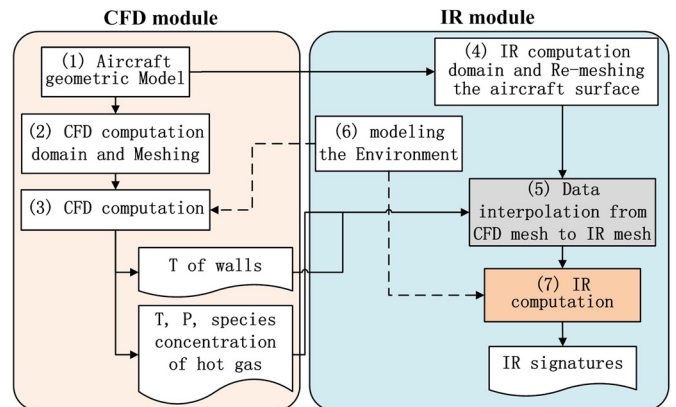**Fig. 1.** The main contributors to the long wave IR signature of an aircraft.

Fig. 2. Computation procedure of aircraft infrared radiation.

(1) conical inner body
(2) first stage of compressor stage
(3) last stage of low pressure turbine
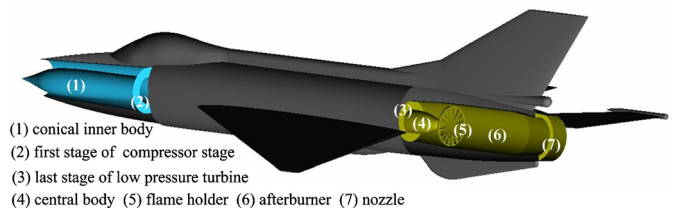(4) central body (5) flame holder (6) afterburner (7) nozzle

Fig. 3. A side view of the aircraft.

to it's temperature above absolute zero degree, but also reflects environmental radiation (such as atmosphere, earth surface and sun). The radiation from sun will also rise the temperature of the airframe surface, and in turn increases the IR signature of an aircraft. All of these factors should be taken into account to calculate the long-wave band IR signature of an aircraft. However, this paper only concentrates on, among various environmental radiations, atmospheric and earth ground radiation. Fig. 1 presents the above-mentioned main sources to the IR signature of an aircraft.

Fig. 2 shows the computation procedure of aircraft infrared radiation, which consists of two modules, CFD module and IR module. The computation procedure is as follows: (1) establishing the aircraft geometric model, (2) meshing the CFD computation domain in facet and volume elements, (3) computing the flow field and the temperature field, (4) meshing the IR computation domain and re-meshing the surface in facet elements, (5) interpolating the CFD data (including the temperature of walls and hot gas flow, as well as the pressure and species concentration of the hot gas flow) to the IR computation mesh, (6) modeling the natural environment, and (7) computing the IR signatures of the aircraft.

2.2. Geometric model

The aircraft geometry model consists of intake cavity, fuselage surface, and engine exhaust cavity, as shown in Fig. 3. The intake
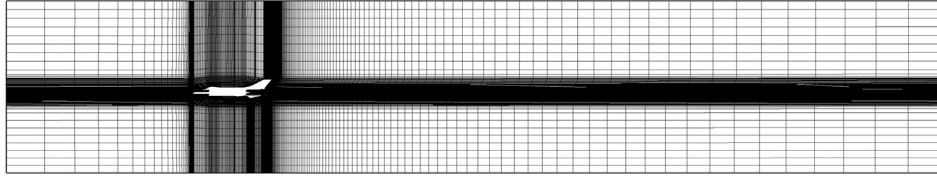
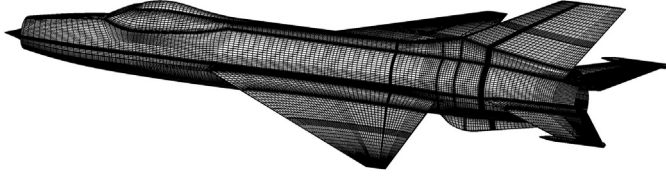**Fig. 4.** The mesh in the symmetry plane of the aircraft.

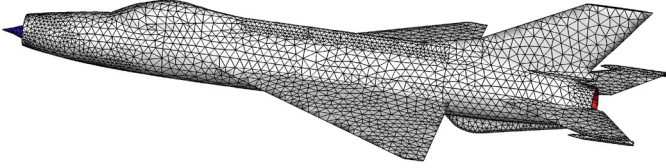**Fig. 5.** The surface mesh of the aircraft for CFD computation.

Fig. 6. The surface mesh of the aircraft for IR computation.

cavity is composed of a flow channel, a conical inner body and a flat plat which represents the first stage of the compressor stage. The exhaust cavity is described by a flat plate which represents the last stage of low pressure turbine blades, a central body, a flame holder, an afterburner and a nozzle. The structure between the first stage of the compressor and the last stage of low pressure turbine is not considered.

2.3. CFD computation domain and meshing

The form of the CFD calculation domain is a semi cylinder. Fig. 4 shows the mesh in the symmetry plane of the aircraft. In the intake cavity, nozzle cavity, plume area and the region near fuselage skin, the volume cells are refined for getting more accurate results of the flow field and temperature filed. Fig. 5 shows the surface mesh of the aircraft for CFD computation, which is a structured rectangular mesh.

Fig. 6 shows the surface mesh of the aircraft for IR radiation computation, which is much coarser than that for CFD computation. It uses triangle surface elements for convenience of calculating the intersection of a ray and the surface elements. The information attached to the IR mesh contains: mesh spatial coordinates, wall element normal direction, parameters of BRDF, emissivity and temperature.

2.4. CFD computation method and boundary conditions

The flow field and the temperature field are computed by using CFD software. The Reynolds-Averaged Navier–Stocks (RANS) equations and scalar equations (energy and species concentration) are solved with the *SST k–ω* model. The gas density is calculated using the ideal gas model. An implicit discretization scheme based on the finite volume method (FVM) is used in the Cartesian coordinate system. The RANS equations, turbulent kinetic energy, k equation, and specific dissipation rate, $ω$ equation, are discretized using the second-order upwind scheme at the cell faces.

The air conditions for CFD computation are showed in Table 1.

At the exit of low pressure turbine of the engine, total temperature and total pressure, T and P, are given as the boundary

Table 1
Pressure and temperature of atmosphere for the CFD computation.

	Summer		Winter	
	P (Pa)	T (K)	P (Pa)	T (K)
7 km	42600	254.7	40160	237.7
11 km	24300	228.8	21990	219.2

Table 2
Pressure and temperature of the engine for the CFD computation.

	Summer		Winter	
	P_t (kPa)	T_t (K)	P_t (kPa)	T_t (K)
7 km	191	1023	213	1053
11 km	120	993	144	1035

condition for hot gas flow field computation, as stated in Table 2. These parameters were estimated via the code, Gas Turb 10, developed by Dr. Joachim Kurzke. For current computation, these data are given in Table 2. The mass fraction of O_2, CO_2, H_2O and N_2 at the exit of low pressure turbine is 14%, 6.8%, 2.7% and 76.5%, respectively.

The material of the aircraft surface is assumed to be aluminum coated with paint, and the thermal characteristics of aluminum were taken in this study. The initial emissivity of the aircraft surface and engine wall is assumed to be 0.85.

2.5. Method of environmental radiation modeling

The radiance of the environment, at the position where the aircraft is located on, is determined by all the radiations from atmosphere and ground, as shown in Fig. 7. The zenith angle ($θ = 0°\sim180°$) is uniformly divided into eighteen directions from the zenith to the nadir, each direction has a zenith angle increment of $Δθ = 10°$. For any zenith angle direction, the environmental radiance in different azimuth angle, $φ$, has the same value. The spectral atmosphere radiance incident on the aircraft, $L_{λ,atmosphere}(θ)$, and transmissivity, $τ_λ(θ)$, are calculated by using the standard code MODTRAN. For the directions ($θ = 0°\sim90°$) above the horizontal plane, only the atmospheric radiation from the top of atmosphere to the position of aircraft needs to be calculated. While for the directions ($θ = 90°\sim180°$) below the horizontal plane, both atmospheric radiation and ground radiation should be considered.

The spectral ground radiance incident on the aircraft, $L_{λ,ground}(θ)$ is:

$$L_{λ,ground}(θ) = τ_λ(θ)\frac{ε_{ground}}{π} \cdot E_b(T_{ground}, λ) \tag{1}$$

where $τ_λ(θ)$ the atmospheric transmissivity between the ground and the aircraft, $ε_{ground}$ is the emissivity of ground, E_b (in W/(m² · μm)) is the black body spectral emissive power [16], which is calculated at the temperature of ground by using Planck law.

$$E_b(T, λ) = \frac{c_1 λ^{-5}}{\exp[c_2/(λT)] - 1} \tag{2}$$

where $c_1 = 3.7418 \times 10^{-16}$ W · m², and $c_2 = 1.4388 \times 10^4$ μm · K.

Two atmospheric IR radiation models, the Mid-latitude Summer and the Mid-latitude Winter, are used in this study. The emissivity
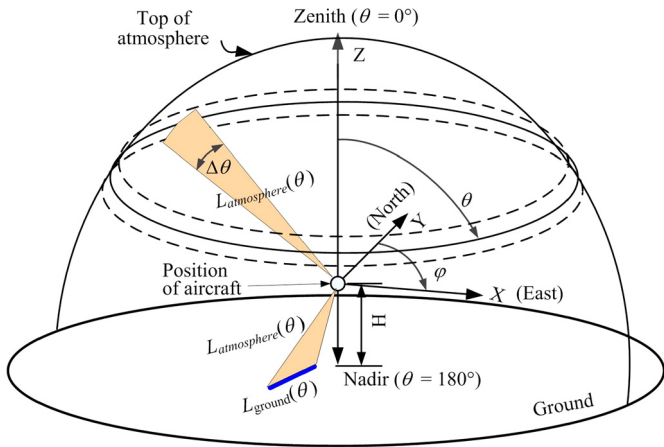
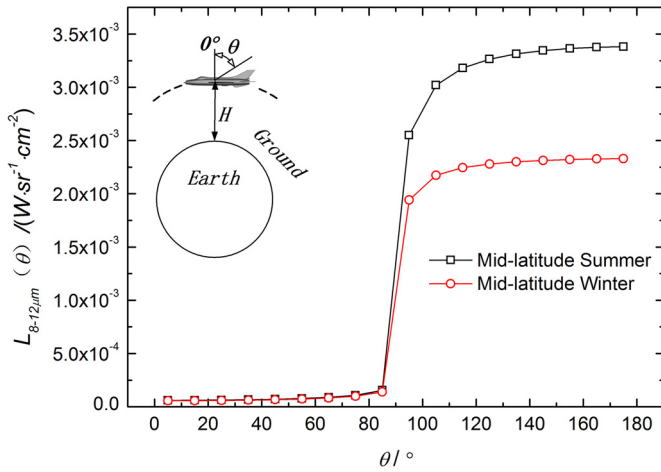Fig. 7. Direction of the environmental radiation according to zenith angle.

Fig. 8. Environmental radiation at the altitude of 11 km.

of ground is assumed to be 0.95. The temperature of the ground surface during summer and winter is assumed to be 294 K and 272 K, respectively. Fig. 8 shows the integral environmental radiation above the aircraft is much less than that below the aircraft at the altitude of 11 km. The difference of the environmental radiance of these two models is pretty small in the angle range of $\theta = 0°$–$90°$ while turns to significant in the zenith angle range of $\theta = 90°$–$180°$.

2.6. The computation method of IR signature of the aircraft

The infrared radiation signature of the aircraft varies with the detection direction. A detection coordinate system with the origin at the gravity center of aircraft is sketched in Fig. 9, where two detection planes, the lateral plane (XOY) and the longitudinal plane (XOZ), are the most interested in this study.

Fig. 10 shows the IR radiation composition on a surface grid element. $\mathbf{n}$ is the normal vector of the skin mesh element, $\mathbf{s}_i$ is the incident vector of environmental radiation in (θ_i, φ_i) direction, dA (in cm^2) is the area of mesh element. $dL_{\lambda,self}$ (in W/(sr · cm^2 · μm)) is the IR radiance of the area element dA in (θ_o, φ_o) direction due to it's self-radiation, $dL_{\lambda,reflect}$ is the reflected environmental IR radiance of the area element dA in (θ_o, φ_o) direction.

The total infrared radiation intensity, $I_{total}(\theta_o, \varphi_o)$ (in W/sr), of the aircraft is showed in equation (3),

$$I_{total}(\theta_o, \varphi_o) = I_{self}(\theta_o, \varphi_o) + I_{reflect}(\theta_o, \varphi_o)$$

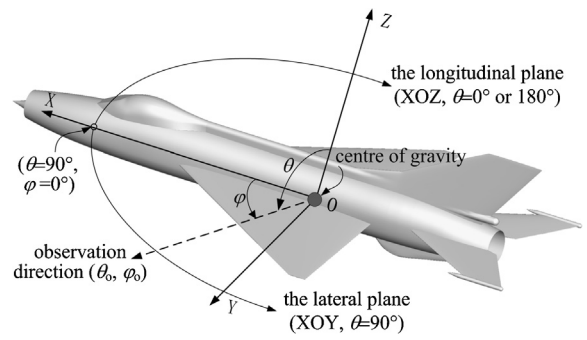Fig. 9. Detection coordinate system.

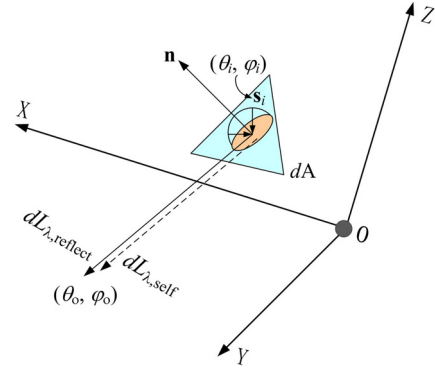Fig. 10. IR radiation composition on a skin grid element.

$$= \int_A \int_{8\,\mu m}^{12\,\mu m} dL_{\lambda,self}(T)d\lambda dA$$

$$+ \int_A \int_{2\pi} \int_{8\,\mu m}^{12\,\mu m} BRDF\big(dL_{\lambda,atmosphere}(\theta_i)$$

$$+ dL_{\lambda,ground}(\theta_i)\big)|\mathbf{n} \cdot \mathbf{s}_i|d\lambda d\Omega dA \quad (3)$$

where A (in cm^2) is the projected area of the aircraft in the detection direction, BRDF (in sr^{-1}) is the bi-directional reflectance distribution function, $d\Omega$ (in sr) is the solid angle of irradiance.

For convenience of discussion, the ratio of reflected environmental infrared radiation intensity to total infrared radiation intensity (RRT for short) is defined as follows,

$$RRT(\theta_o, \varphi_o) = I_{reflect}(\theta_o, \varphi_o)/I_{total}(\theta_o, \varphi_o) \times 100\% \quad (4)$$

The Reverse Monte Carlo ray tracing method (RMC) was employed to calculate the total radiation intensity. Fig. 11 illustrates the reverse Monte Carlo ray tracing. The target plane is divided into many small regions. The basic idea of RMC is to emit a huge number of rays from the detector in the field of view (FOV), and then tracing the destination of each ray with statistical criterions. If the ray is absorbed by a surface element or a gas element of the computation domain, it means that there is a real ray emits from the absorbed location and travels along the reverse direction to the detector. And the reverse ray carries a radiant energy determined by the temperature and the emissivity of the surface element or the gas element. If the ray is reflected by the surface element and goes into the environment, it means that the radiant energy carried back by a reverse ray is the environmental infrared radiation. Detailed calculation process is showed as follows.

First, the input data are prepared, including: 1) the coordinates and normal vector direction of aircraft surface elements, temperature and parameters of BRDF of each element; 2) the coordinates
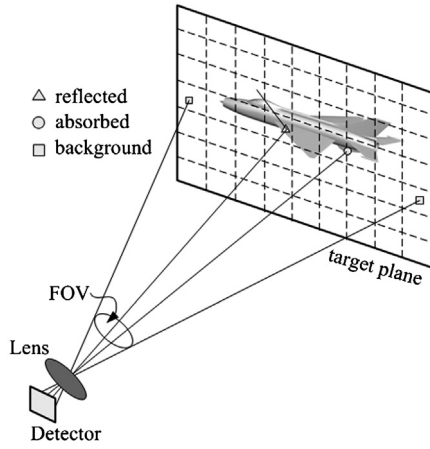
Fig. 11. Illustration of the reverse Monte Carlo ray tracing.

Fig. 12. The comparison of apparent infrared radiance between calculated and measured one.

of the plume grids, pressure profiles, temperature profiles and H_2O concentration profiles; 3) absorption coefficients and spectral line density data of H_2O.

Then, a ray is fired from the detector to the target plane. When the ray reaches the surface, it will either be absorbed or reflected, which are determined by a random number *RAN* with a uniform probability distribution between 0 and 1. The probability of the event is proportional to the emissivity, ε, of the surface. If *RAN* is larger than ε, the event of reflection is occurred, or else absorption is occurred. The direction of the reflected ray is determined by BRDF. One of the most popular BRDF model, the modified Phong model [17], which can be written as the sum of a diffuse part and a specular part, is used here.

$$BRDF(\theta_i, \varphi_i, \theta_o, \varphi_o) = \frac{k_d}{\pi} + \frac{k_s}{2\pi}(n+2)\cos^n \alpha \qquad (5)$$

where, θ_i and φ_i are the elevation angle and the azimuth angle of the incoming ray, respectively, θ_o and φ_o are the elevation angle and azimuth angle of the outgoing ray, respectively, k_d is the diffuse reflectivity, k_s is the specular reflectivity, n is the specular exponent, α is the angle between the viewing vector and the perfect mirror-like reflection vector. In this study, k_d equals to k_s, and take $(1-\varepsilon)/2$, where ε is the normal emissivity of the aircraft surface, and n takes 50.

When a ray reaches the plume, it will either pass through or be absorbed. The probability of the occurrence of each event is related to both the absorptivity, α_λ, and another random number *RAN* with a uniform probability distribution between 0 and 1. If *RAN* is larger than α_λ ($=1-\bar{\tau}_\lambda$, where $\bar{\tau}_\lambda$ is the transmissivity averaged over a spectral interval), the ray passes through the medium. Otherwise, the ray is absorbed by the medium. The Malkmus [18] model was used to calculate the gas transmissivity. This model is recognized as a suitable Statistical Narrow-Band (SNB) model for combustion gases. Three major assumptions are applied to this model: randomness of line locations, Lorentz line shape, and exponential distribution of line intensity. The average transmissivity [19] over a spectral interval of the combustion gas of length l (in cm), pressure p (in atm), and molar fraction x is

$$\bar{\tau} = \exp\left[-2\frac{\gamma}{\delta}\left(\sqrt{1 + xpl\bar{\kappa}\frac{\bar{\delta}}{\gamma}} - 1\right)\right] \qquad (6)$$

where γ (in cm^{-1}) is the half-width of the lines of the absorbing gas, $1/\bar{\delta}$ (in cm) is the line density, $\bar{\kappa}$ is the absorption coefficient (in $cm^{-1} \cdot atm^{-1}$).

Lastly, the radiant energy carried back to the detector along the reverse direction of the ray is calculated. If the ray is absorbed by the hot gas or aircraft surface, the infrared radiance is,
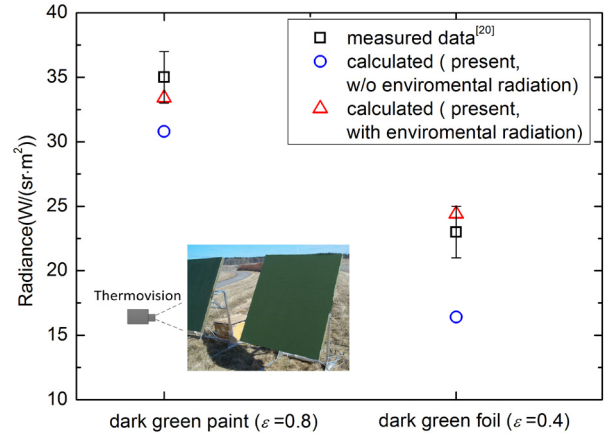
$$L_{\lambda,self}(T) = \frac{E_b(T, \lambda)}{\pi} \qquad (7)$$

where T is the temperature of the gas or the wall at the position of absorption.

If the ray is reflected to the environment, the infrared radiance is $L_{\lambda,atmosphere}(\theta_i)$ or the sum of $L_{\lambda,ground}(\theta_i)$ and $L_{\lambda,atmosphere}(\theta_i)$.

3. Validation of the infrared radiation computation

Validation of the computation method of infrared radiation with environmental radiation is carried out by comparing the computation results of plates radiations with the experimental data of Hermansson [20]. The experimental measurements were made at two different plates, the first one was painted with dark green paint which has an emissivity of 0.8 and temperature of 32 °C, and the second one was covered with dark green foil which has an emissivity of 0.4, and temperature of 36 °C. A THV900 thermovision camera with filter LPL (7.5~12 μm) was used to measure the apparent radiance and the apparent temperature of the two plates. More information about the thermovision camera and experimental condition could be found in reference [20]. The geographic position of the measurement was at N58°, therefore the subarctic atmosphere model was used in the computation to simulate the experimental environment.

Fig. 12 shows the comparison of the apparent infrared radiance between calculated and measured one. It can be seen that, if the environmental radiation is not considered, there is an obvious deviation between the calculated data (marked with symbol ○) and measured data (marked with symbol □). If the environmental radiation is considered, the deviation is evidently reduced. The infrared radiation for low emissivity panel is over predicted whereas under predicted infrared radiation in case of high emissivity panel. One possible reason is that the emissivity is not accurate. If the emissivity of the low emissivity panel is reduced from 0.4 to 0.3, we will slightly under predict infrared radiation compared to measured infrared radiation for low emissivity panel.

Fig. 13 shows the comparison of the apparent infrared radiation temperature between calculated and measured one. The calculated temperatures of the two plates are also in good agreement with the measurement. These comparisons show that the reflected environmental radiation increases the total radiance of the plates, and the reflected environmental radiation of a low emissivity surface is higher than that of a high emissivity surface.

It should be noted that the environment IR radiation is very complex, and it is difficult to guarantee that the computation model is competent to all the real situations.
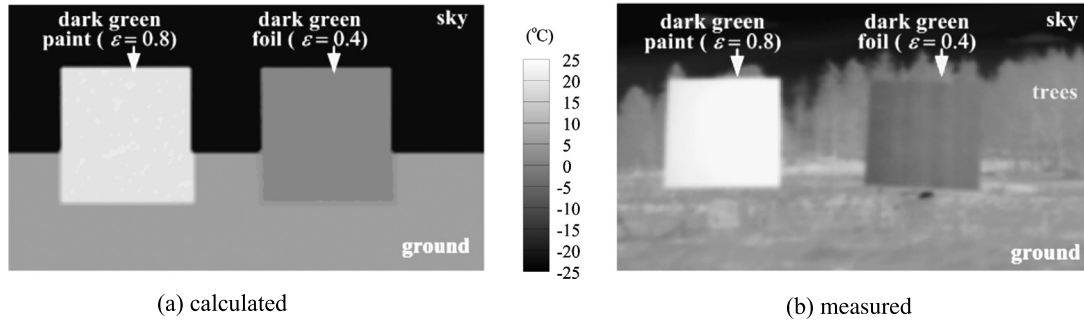
(a) calculated

(b) measured

Fig. 13. The comparison of the apparent temperature between calculated and measured one.
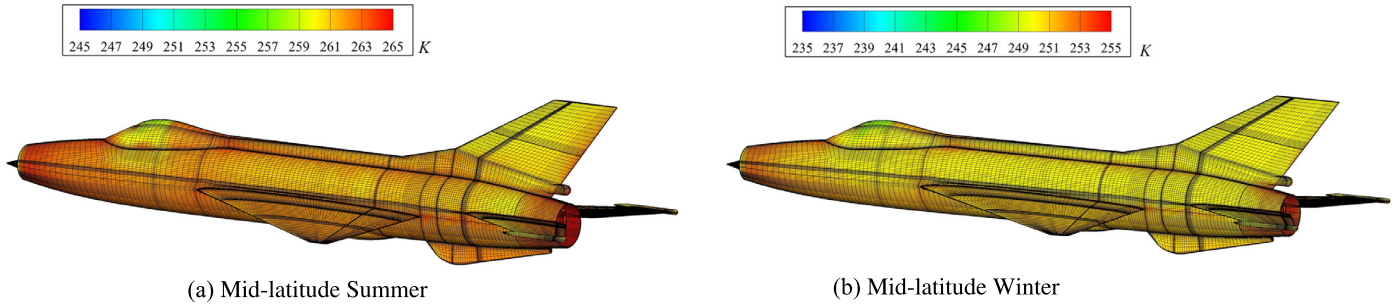

(a) Mid-latitude Summer

(b) Mid-latitude Winter

Fig. 14. Temperature of the aircraft surface ($H = 11$ km, $Ma = 0.9$). (For interpretation of the colors in this figure, the reader is referred to the web version of this article.)
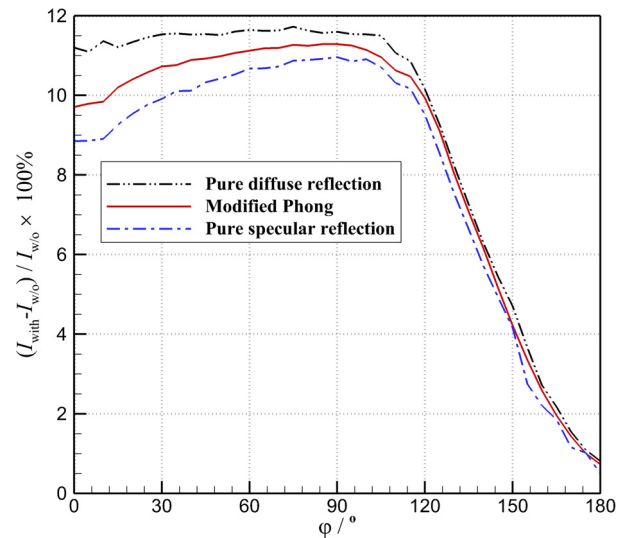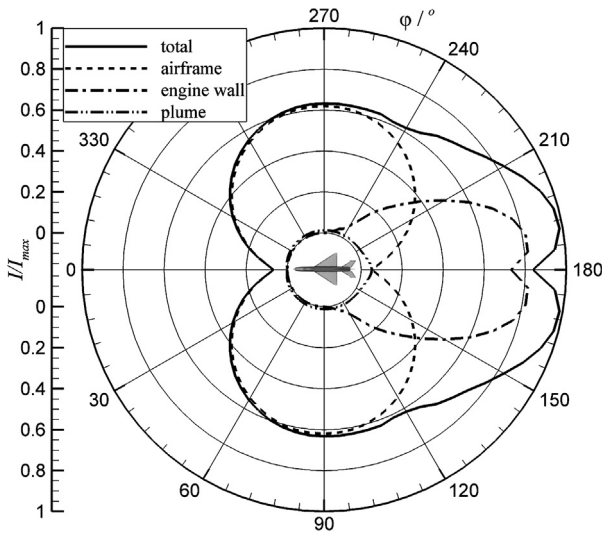

Fig. 15. Distribution of the non-dimensional infrared radiation intensity (without environmental radiation) in XOY plane (Mid-latitude Summer, $H = 11$ km, $Ma = 0.9$).

Fig. 16. The effect of reflected environmental radiation on the IR signature of aircraft in XOY plane (Mid-latitude Summer, $H = 11$ km, $Ma = 0.9$).

4. Results and discussion

4.1. Distribution of the temperature of the aircraft surface

Fig. 14 shows the distribution of the temperature of the aircraft surface. It can be observed that the predicted aircraft temperature with RANS method varies with spatial location. This is mainly caused by the state of the external flow near the surface. If using the total temperature of the incoming airflow and empirical formula to estimate the recovery temperature of the aircraft, one can only get an overall average temperature, and this may lead to a larger computation error of IR signature of the aircraft.

The temperature distribution of Fig. 14(b) is similar to that of Fig. 14(a), however, the overall amplitude of Fig. 14(b) is lower than Fig. 14(a). The difference is about 11 K.

4.2. Spatial distribution of infrared signature of the aircraft

Fig. 15 shows the spatial distribution of the non-dimensional infrared radiation intensity (without considering the environmental radiation) in the XOY plane. I_{max} is the maximum infrared radiation intensity of the aircraft under the condition of Mid-latitude Summer, $H = 11$ km and $Ma = 0.9$. In this plane, the distribution of non-dimensional infrared radiation intensity is symmetrical about x-axis, so in the following discussion only the spatial distribution in the range of $\varphi = 0°–180°$ is discussed. In the front and side detection range ($\varphi = 0°–120°$), the main radiation source is the airframe. In the rear detection range ($\varphi = 150°–180°$), the main radiation source is the engine wall. Since H_2O has no strong emission and CO_2 nearly has no emission in the long-wave band, the plume radiation in this waveband is relatively weak ($<5\%$). For this reason, the contribution of gas radiation in long-wave band to
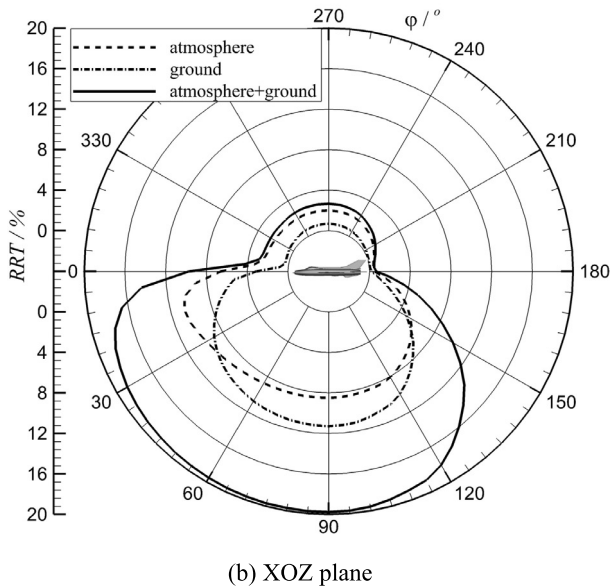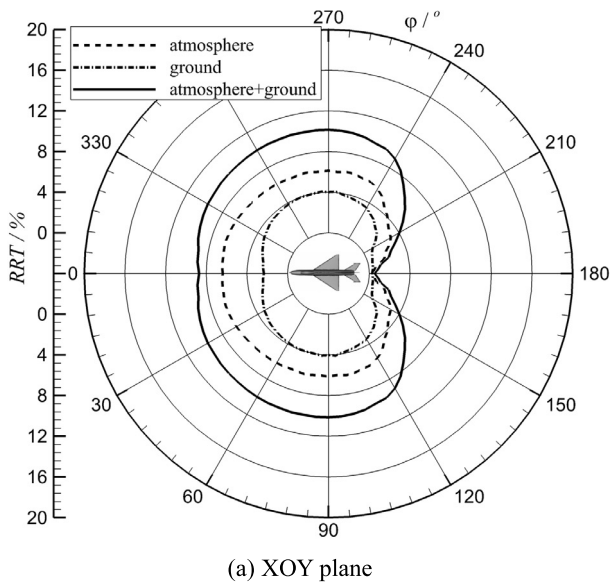
(a) XOY plane

(a) XOY plane

(b) XOZ plane

(b) XOZ plane

Fig. 17. Spatial distribution of RRT in XOY plane and XOZ plane (Mid-latitude Summer, $H = 11$ km, $Ma = 0.9$).

Fig. 18. The effect of season on the spatial distribution of RRT in XOY plane and XOZ plane ($H = 11$ km, $Ma = 0.9$).

infrared signature of aircraft will be omitted in the following discussion.

Fig. 16 shows the effect of reflected environmental radiation on IR signature of the aircraft, where $(I_{with} - I_{w/o})$ is the difference between the infrared radiation intensity with and without considering the environmental radiation. The calculations of infrared radiation are made with three reflection models: the diffuse model, the specular model and the modified Phong BRDF model. The results show that the total infrared radiation of the aircraft is increased by considering the environmental radiation. The amplitude of the increase calculated with the modified Phong BRDF model is between those calculated with diffuse reflection model and specular reflection model. Therefore, in this paper hereafter, all the results are computed with the modified Phong BRDF model. It also can be seen that in the region of $\varphi = 0°$–$120°$, the IR radiation intensities with environmental radiation are 10%–11% larger than that without environmental radiation. In the region of $\varphi = 120°$–$180°$, the ratio decreases with the φ increasing.

Fig. 17 shows the spatial distribution of RRT in XOY plane and XOZ plane. The RRT distribution is symmetrical in XOY plane,

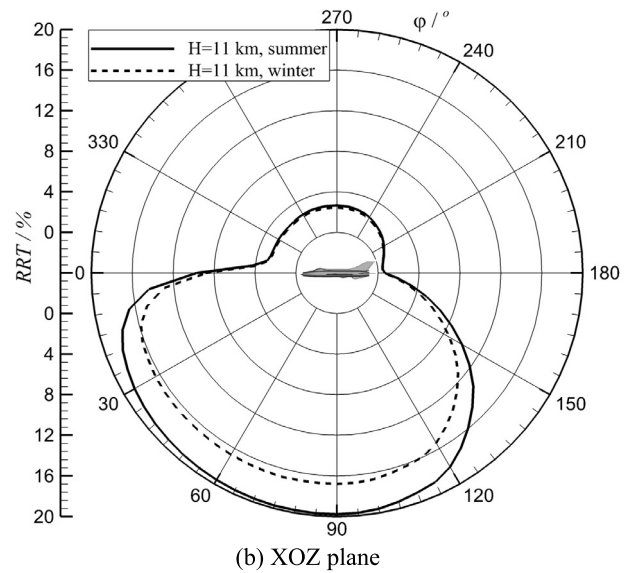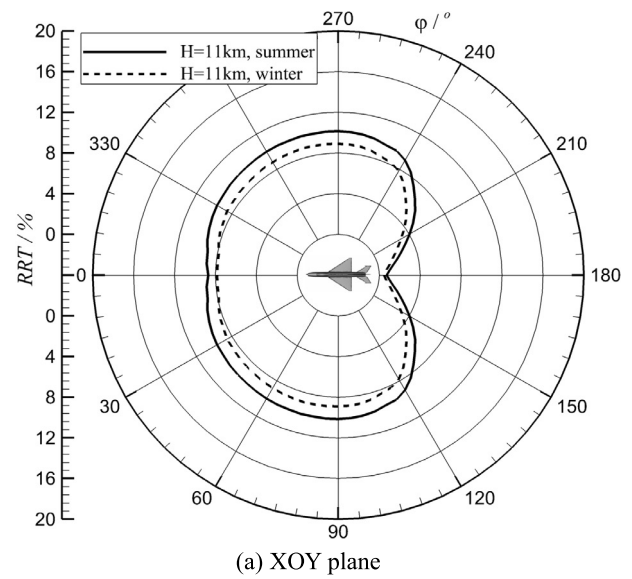while asymmetrical in XOZ plane. In the XOY plane, the RRT due to atmospheric radiation (about 6%) is larger than that due to ground radiation (about 4%). In the lower semi-circle of XOZ plane ($\varphi = 0°$–$180°$), the effect of environmental radiation on the aircraft IR signature is more significant than that in the upper semi-circle of the XOZ plane ($\varphi = 180°$–$360°$). The maximum value of RRT due to atmospheric radiation is about 10% and appears in the detection region of $\varphi = 5°$–$30°$. The maximum value of RRT due to ground radiation appears in the straight downward direction, and it takes about 11%.

The reflected environmental radiation (sum of atmospheric radiation and ground radiation) accounts for about 20% of the total radiation of a aircraft in the straight downward direction, while about 10% of the total radiation in the side detection direction ($\varphi = 90°$).

Fig. 18 shows the effect of season on the spatial distribution of RRT in XOY plane and XOZ plane. It can be seen that the effect of environmental radiation in winter is a little smaller than that in summer. In the XOY plane, the RRT in winter is about 0.9 times as much as that in summer. In the XOZ plane, the RRT of
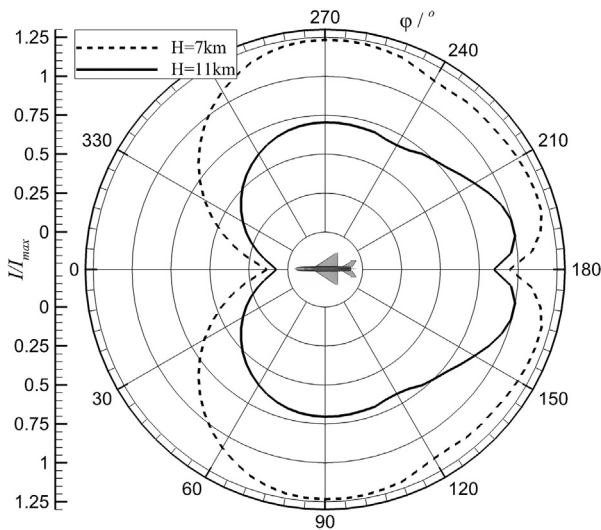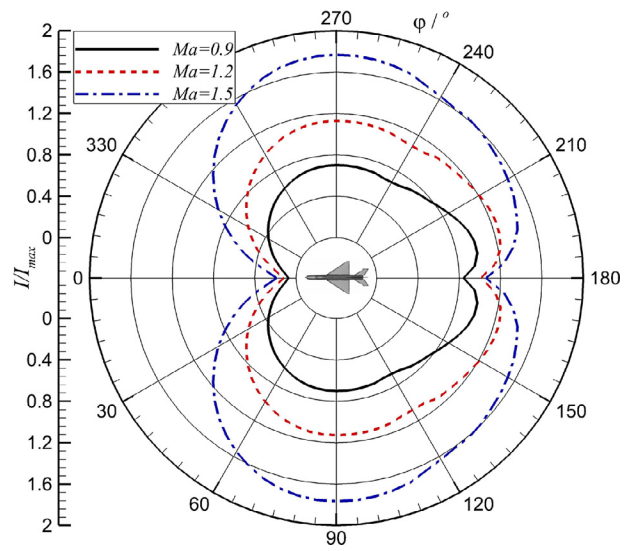
Fig. 19. The non-dimensional IR signature of the aircraft at two different flight altitudes in the XOY plane (Mid-latitude Summer, $Ma = 0.9$, 8–12 μm).
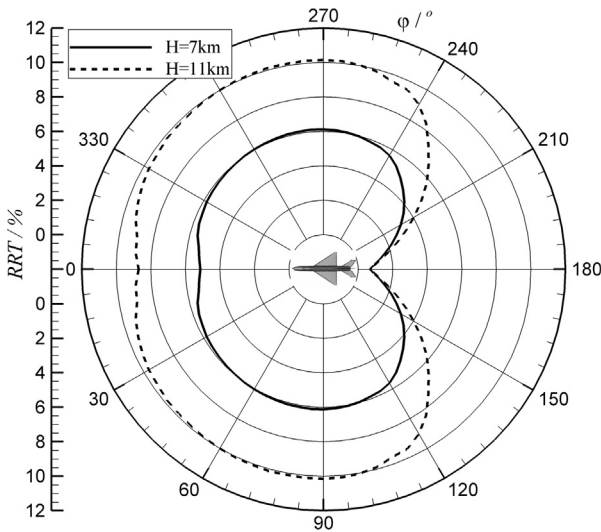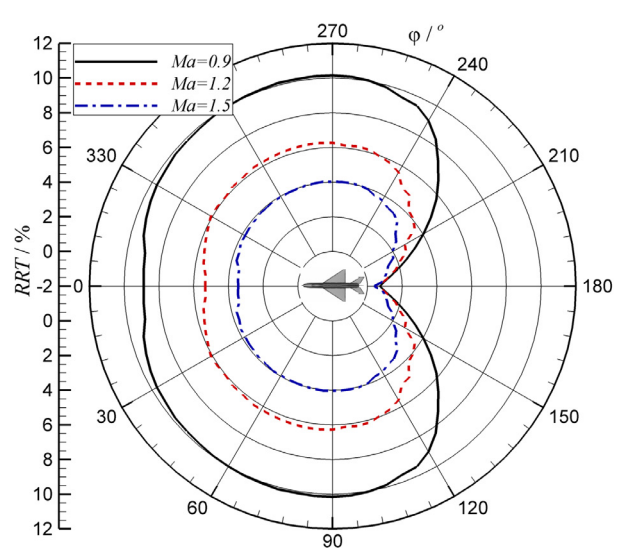

(a) Non-dimensional IR radiation intensity

Fig. 20. The spatial distribution of RRT at two different flight altitudes in the XOY plane (Mid-latitude Summer, $Ma = 0.9$, 8–12 μm).

(b) RRT

Fig. 21. The spatial distribution of the non-dimensional IR radiation intensity and RRT of the aircraft at three flight speeds under the condition of Mid-latitude Summer ($H = 11$ km, 8–12 μm).

$\varphi = 180°$–$360°$ in winter is nearly the same as that in summer, however, the RRT of $\varphi = 0°$–$180°$ in winter is obviously smaller than that in summer. The RRT of $\varphi = 90°$ in winter is about 0.85 times as much as that in summer. Hereafter, we will only discuss the results of summer.

4.3. The effect of flight altitude and environmental radiation on the aircraft IR signature

Fig. 19 shows the non-dimensional IR signature of the aircraft flying at Mach 0.9 and altitude of 7 km and 11 km. Since the atmosphere temperature at 11 km is lower than that at 7 km, the aircraft infrared radiation intensity at 7 km is stronger than that at 7 km. In the detection region of $\varphi = 0°$–$120°$, the infrared intensity of aircraft at 7 km is about 70% larger than that at 11 km.

Fig. 20 shows the spatial distribution of RRT in XOY plane at these two flight altitudes. In the detection range of $\varphi = 0°$–$120°$, the RRT of the aircraft is about 9%–10% at 11 km, and about 5%–6% at 7 km. In the detection range of $\varphi = 120°$–$240°$, the RRT is small because the total radiation is dominated by the engine exhaust wall radiation.

4.4. The effect of flight speed and environmental radiation on the aircraft IR signature

Fig. 21 shows the spatial distribution of the non-dimensional IR radiation intensity and RRT of the aircraft flying at altitude of 11 km and Mach number of 0.9, 1.2 and 1.5 under the condition of Mid-latitude Summer. It can be seen that the effect of the environmental radiance in the detection range of $\varphi = 0°$–$120°$ is more obvious than that of $\varphi = 120°$–$180°$. The RRT is related to the flight speed, the higher the speed, the lower the RRT. In the detection range of $\varphi = 0°$–$120°$, the mean RRT is about 9.7%, 6.0%, and 3.8% for $Ma = 0.9$, $Ma = 1.2$, and $Ma = 1.5$, respectively.

4.5. The effect of emissivity of the airframe surface and environmental radiation on the aircraft IR signature

Fig. 22 shows the spatial distribution of infrared radiation intensity of aircraft with three different emissivities (0.85, 0.6 and 0.35). It can be seen that, if the reflection of the environmental
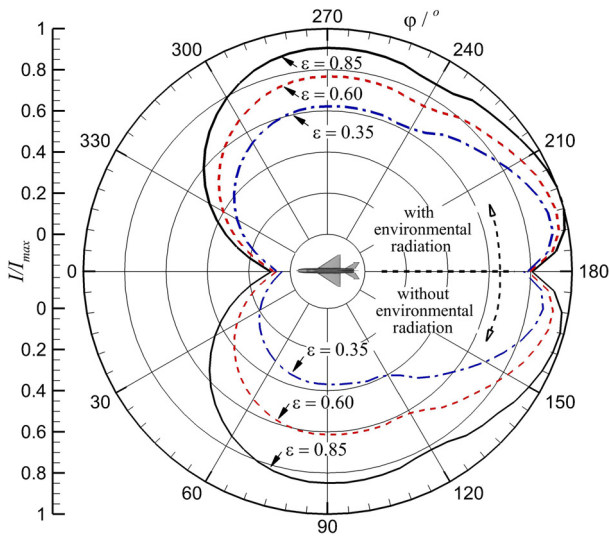
Fig. 22. Infrared radiation intensity of aircraft with three different emissivities ($Ma = 1.2$, $H = 11$ km, Mid-latitude summer).

radiation is not considered, low emissivity surface can reduce the infrared signature of aircraft significantly. The emissivity decreases from 0.85 to 0.35, the IR radiation intensity of the aircraft side direction will decrease by 57%. If the reflection of the environmental radiation is considered, the amplitude of infrared radiation intensity reduction caused by low emissivity surface will reduce, evidently. The emissivity decreases from 0.85 to 0.35, the IR radiation intensity of the aircraft side direction will only decrease by

31%. The main reason is that the low emissivity surface reflects more environmental radiation. Since the emissivity of the engine exhaust cavity is kept constant in this three cases, therefore, the decrease of the IR radiation with aircraft surface emissivity in the rear view is not obvious.

Fig. 23 shows the calculated long-wave band thermal images of the aircraft viewed from a left-front direction of the aircraft. If the reflection of the environmental radiation is not considered (see Fig. 23 (a), (c), and (e)), the radiation temperature decreases with the reduction of the emissivity, and the thermal image of the aircraft merges with the sky background when $\varepsilon = 0.35$. While if the reflection of the environmental radiation is considered (see Fig. 23 (b), (d), and (f)), the radiation temperature of the aircraft is significantly higher than that without considering the environmental radiation. Even though the emissivity is as low as 0.35, the temperature of the aircraft is still much higher than the background, especially for the lower surface of the aircraft.

5. Conclusions

The reflected environmental radiance is an important part of the aircraft infrared signature in the long-wave band. The effect of the reflected environmental radiation on the infrared signature of a cruise aircraft is related to the atmosphere condition, the flight speed, the flight height, and the emissivity of the airframe surface. The effect of atmospheric radiation on the infrared signature of the lower part of the longitudinal detection plane is the largest, followed by the lateral detection directions and the upper part of the longitudinal detection directions. The effect of reflected ground radiation on the infrared signature of aircraft is similar to that
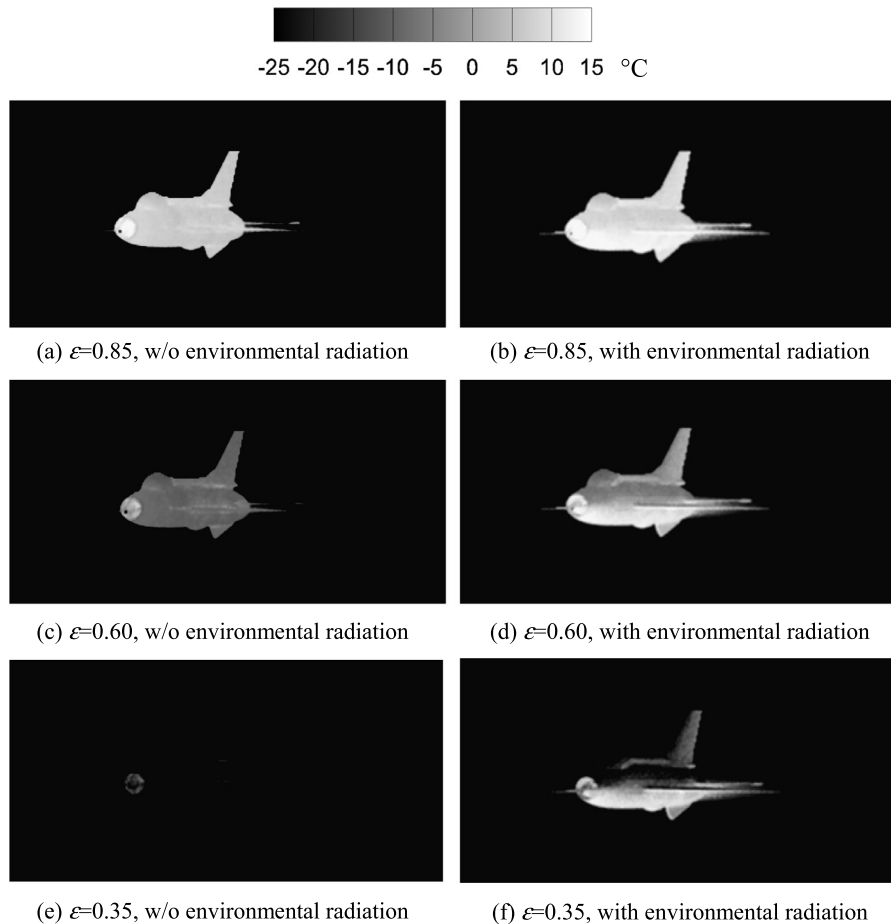

(a) ε=0.85, w/o environmental radiation

(b) ε=0.85, with environmental radiation

(c) ε=0.60, w/o environmental radiation

(d) ε=0.60, with environmental radiation

(e) ε=0.35, w/o environmental radiation

(f) ε=0.35, with environmental radiation

Fig. 23. The calculated thermal images of the aircraft viewed from a left-front direction ($Ma = 1.2$, Mid-latitude summer)

of atmosphere radiation. Increasing flight altitude (from 7 km to 11 km), reducing atmosphere temperature (from summer to winter) and reducing flight speed will increase the RRT (ratio of reflected environmental infrared radiation intensity to total infrared radiation intensity) of aircraft. The reflected environmental radiance (sum of atmospheric radiance and ground radiance) accounts for more than 20% of the total radiation of a basic aircraft with a speed of Mach 0.9 in the straight downward direction, and more than 10% of the total radiation in the lateral detection directions.

The computational results show that the long-wave band radiation temperature of the aircraft decreases significantly with the reduction of the surface emissivity. But the amplitude of reduction is reduced if the environmental radiation is considered. For an aircraft flying at Mach 1.2, if airframe surface emissivity decreases from 0.85 to 0.35, the reduction amplitude with considering the environmental radiation is about 54% of that without considering the environmental radiation. The radiation temperature of the aircraft lower surface is still significantly higher than that of the aircraft upper surface and background, even though the emissivity of the aircraft surface is as low as 0.35.

Conflict of interest statement

Acknowledgements

References

[1] E. Coiro, Global illumination technique for aircraft infrared signature calculations, J. Aircr. 50 (1) (2013) 103–113.

[2] S.P. Mahulikar, H.R. Sonawane, G.A. Rao, Infrared signature studies of aerospace vehicles, Prog. Aerosp. Sci. 43 (7) (2007) 218–245.

[3] M. Wilson, R. Elliott, K. Youern, The use of measured sky radiance data to improve infrared signature modelling, Int. J. Remote Sens. 29 (7) (2008) 1929–1944.

[4] W.R. Bliss, Atmospheric radiation near the surface of the ground, Sol. Energy 5 (1961) 103–120.

[5] B.A. Kimball, S.B. Idso, J.K. Aase, A model of thermal-radiation from partly cloudy and overcast skies, Water Resour. Res. 18 (1982) 931–936.

[6] C.N. Awanou, Clear sky emissivity as a function of the zenith direction, Renew. Energy 13 (2) (1998) 227–248.

[7] X. Berger, A simple model for computing the spectral radiance of clear skies, Sol. Energy 40 (4) (1988) 321–333.

[8] X. Berger, J. Bathiebo, Directional spectral emissivities of clear sky, Renew. Energy 28 (12) (2003) 1925–1933.

[9] A. Berk, L.S. Bernstein, D.C. Robertson, MODTRAN: a moderate resolution model for LOWTRAN 7, AFGL-TR-89-0122, 1989.

[10] S.P. Mahulikar, S.K. Potnuru, G.A. Rao, Study of sunshine, skyshine, and earthshine for aircraft infrared detection, J. Opt. A, Pure Appl. Opt. 11 (4) (2009) 045703–045712.

[11] M.F. Modest, Radiative Heat Transfer, second edition, Academic Press, San Diego, USA, 2003.

[12] S.I. Harkiss, A study of bi-directional reflectance distribution functions and their effect on infrared signature models, AFIT/GE/ENP/07-01, 2007.

[13] N. Li, Z. Su, Z. Chen, D. Han, A real-time aircraft infrared imaging simulation platform, Optik 124 (2013) 2885–2893.

[14] G.A. Rao, S.P. Mahulikar, Effect of atmospheric transmission and radiance on aircraft infrared signatures, J. Aircr. 42 (4) (2005) 1046–1054.

[15] J. Lü, Q. Wang, Aircraft-skin infrared radiation characteristics modeling and analysis, Chin. J. Aeronaut. 22 (5) (2009) 493–497.

[16] M.F. Modest, Radiative Heat Transfer, third edition, Academic Press, Boston, 2013.

[17] B. Balling, A comparative study of the bidirectional reflectance distribution function of several surfaces as a mid-wave infrared diffuse reflectance standard, AFIT/GE/ENP/09-M01, 2009.

[18] W. Malkmus, Random Lorentz band model with exponential-tailed S^{-1} line-intensity distribution function, J. Opt. Soc. Am. 57 (3) (1967) 323–329.

[19] A. Soufiani, J. Taine, High temperature gas radiative property parameters of statistical narrow-band model for H_2O, CO_2 and CO, and correlated-K model for H_2O, CO_2, Int. J. Heat Mass Transf. 40 (4) (1997) 987–991.

[20] P. Hermansson, A. Hjelm, R. Lindell, Benchmarking and validation of IR signature programs: SensorVision, CameoSim and RadThermIR, FOI-R-0952-SE, 2003.